

A *SUZAKU* SEARCH FOR NON-THERMAL EMISSION AT HARD X-RAY ENERGIES IN THE COMA CLUSTER

DANIEL R. WIK¹, CRAIG L. SARAZIN¹, ALEXIS FINOGENOV^{2,3}, KYOKO MATSUSHITA⁴, KAZUHIRO NAKAZAWA⁵, TRACY E. CLARKE^{6,7}

Draft version November 8, 2018

ABSTRACT

The brightest cluster radio halo known resides in the Coma cluster of galaxies. The relativistic electrons producing this diffuse synchrotron emission should also produce inverse Compton emission that becomes competitive with thermal emission from the ICM at hard X-ray energies. Thus far, claimed detections of this emission in Coma are controversial (e.g., Fusco-Femiano et al. 2004; Rossetti & Molendi 2004). We present a *Suzaku* HXD-PIN observation of the Coma cluster in order to nail down its non-thermal hard X-ray content. The contribution of thermal emission to the HXD-PIN spectrum is constrained by simultaneously fitting thermal and non-thermal models to it and a spatially equivalent spectrum derived from an *XMM-Newton* mosaic of the Coma field (Schuecker et al. 2004). We fail to find statistically significant evidence for non-thermal emission in the spectra, which are better described by only a single or multi-temperature model for the ICM. Including systematic uncertainties, we derive a 90% upper limit on the flux of non-thermal emission of 6.0×10^{-12} erg s⁻¹ cm⁻² (20-80 keV, for $\Gamma = 2.0$), which implies a lower limit on the cluster-averaged magnetic field of $B > 0.15 \mu\text{G}$. Our flux upper limit is $2.5 \times$ lower than the detected non-thermal flux from *RXTE* (Rephaeli & Gruber 2002) and *BeppoSAX* (Fusco-Femiano et al. 2004). However, if the non-thermal hard X-ray emission in Coma is more spatially extended than the observed radio halo, the *Suzaku* HXD-PIN may miss some fraction of the emission. A detailed investigation indicates that ~ 50 – 67% of the emission might go undetected, which could make our limit consistent with Rephaeli & Gruber (2002) and Fusco-Femiano et al. (2004). The thermal interpretation of the hard Coma spectrum is consistent with recent analyses of *INTEGRAL* (Eckert et al. 2007a) and *Swift* (Okajima et al. 2008; Ajello et al. 2009) data.

Subject headings: galaxies: clusters: general — galaxies: clusters: individual (Coma) — intergalactic medium — magnetic fields — radiation mechanisms: non-thermal — X-rays: galaxies: clusters

1. INTRODUCTION

In the hierarchical scenario of cosmic structure formation, clusters of galaxies form at late times through mergers between subclusters and through the accretion of galaxies and galaxy groups. The distribution of their massive halos in space and time depend sensitively on the underlying cosmology, and much effort has been made to connect observable properties of the gas to the total cluster mass in order to constrain cosmological parameters (e.g., Mantz et al. 2008, and references therein). However, merger processes are known to significantly disrupt the thermal gas (e.g. Ricker & Sarazin 2001; Ritchie & Thomas 2002), typically biasing inferred masses and the resultant cosmological parameter estimates (Randall et al. 2002; Wik et al. 2008). Merger-induced shocks and turbulence, besides heating the gas, are thought to also re-accelerate relativistic particles present in the intracluster medium (ICM) (Sarazin 1999; Brunetti & Blasi 2005). Non-thermal electrons, observed via diffuse, radio synchrotron emission, have been detected in over 50 clusters, all of them undergoing mergers (Buote 2001; Schuecker et al. 2001). If the energy in a relativistic phase of the ICM is large enough to add pressure support to the thermal

gas, even transiently, the ability to derive masses and therefore use clusters as cosmological probes may be compromised (Skillman et al. 2008). An assessment of the relativistic contribution to the energy budget of clusters is necessary to fully characterize the state of the ICM.

Diffuse, cluster-wide synchrotron radio emission, called radio halos or relics depending on their morphology, imply that both magnetic fields and relativistic electron populations are present on large scales. The total luminosity of a synchrotron-emitting electron is given by

$$L_R = \frac{4}{3} \sigma_T c \gamma^2 \epsilon_B, \quad (1)$$

where σ_T is the Thomson cross-section, c is the speed of light, γ is the Lorentz factor of the electron, and $\epsilon_B = B^2/8\pi$ is the energy density of the magnetic field. For many such electrons, the value of L_R depends both on the number of electrons and on B and cannot independently determine either. However, these same electrons will up-scatter cosmic microwave background (CMB) photons through inverse Compton (IC) interactions, which have a luminosity L_X equivalent in form to equation (1) but with ϵ_B replaced by the energy density of the CMB. Since both luminosities are proportional to the number of electrons, their ratio gives the volume-averaged magnetic field,

$$\frac{L_R}{L_X} = \frac{B^2/8\pi}{aT_{CMB}^4}, \quad (2)$$

where a is the radiation constant and T_{CMB} is the temperature of the CMB. The IC radiation should be observable at hard X-ray energies (Rephaeli 1977). Thus far, IC emission

arXiv:0902.3658v1 [astro-ph.CO] 20 Feb 2009

¹ Department of Astronomy, University of Virginia, P. O. Box 400325 Charlottesville, VA 22904-4325; drw2x@virginia.edu

² Max Planck Institute for Extraterrestrial Physics

³ Center for Space Science Technology, University of Maryland Baltimore County

⁴ Department of Physics, Tokyo University of Science

⁵ Physics Department, University of Tokyo

⁶ Naval Research Laboratory

⁷ Interferometrics Inc.

has only been detected at low significance (Nevalainen et al. 2004) or, in one case, in a cluster with uncertain radio emission (Eckert et al. 2008; but see also Ajello et al. 2009 and Fujita et al. 2008). The measurement of an IC flux from a synchrotron source directly leads to a simultaneous determination of the average value of B and the relativistic electron density (Harris & Romanishin 1974; Sarazin 1988). Therefore searches for IC emission coincident with a radio halo or relic are an excellent way to constrain the contribution of relativistic materials in clusters.

The first, and brightest, radio halo was discovered by Willson (1970) in the Coma cluster, and its radio properties have perhaps been the best studied (e.g. Giovannini et al. 1993; Deiss et al. 1997; Thierbach et al. 2003). Coma has been observed by all the major observatories with hard X-ray capabilities (Rephaeli et al. 1994; Hughes et al. 1993; Bazzano et al. 1990; Henriksen & Mushotzky 1986), and more recently non-thermal detections have been claimed by Rephaeli & Gruber (2002) with *RXTE* and by Fusco-Femiano et al. (1999, 2004) with *BeppoSAX*, though the latter detection is controversial (Rossetti & Molendi 2004; Fusco-Femiano et al. 2007). Due to the large field of view (FOV) of these non-imaging instruments and the simple characterization of the thermal gas, the source of this emission remains uncertain. Even more recently, long (~ 1 Msec) observations with *INTEGRAL* have imaged extended diffuse hard X-ray emission from Coma, though it was found to be completely consistent with thermal emission (Renaud et al. 2006; Eckert et al. 2007a; Lutovinov et al. 2008).

In this study, we present a *Suzaku* HXD-PIN observation of the Coma cluster in an effort to detect non-thermal emission associated with the radio halo and potentially confirm the *RXTE* and *BeppoSAX* detections. The HXD-PIN instrument has a non-imaging collimator like those on-board *RXTE* and *BeppoSAX*, but with a FOV about a quarter as large, which reduces the possible contamination from hard point sources (Takahashi et al. 2007). Also, the *Suzaku* particle background is $\sim 5\times$ lower than the backgrounds of either *RXTE* or *BeppoSAX* (Mitsuda et al. 2007). In order to clearly distinguish the thermal and non-thermal emission visible within the PIN, the hard *Suzaku* PIN spectrum is jointly fit with a spatially equivalent *XMM-Newton* EPIC-pn spectrum. The *XMM* spectrum, at lower energies and completely dominated by thermal emission, allows Coma's thermal and non-thermal properties to be simultaneously determined. The *XMM* and HXD-PIN observations are reported in § 2 and the extraction of the resulting spectra is discussed in § 3. Fits to the joint spectra are described in § 4. In § 5, we discuss the implications of our results for the nature of the hard X-ray emission from the Coma cluster. We assume a flat cosmology with $\Omega_M = 0.23$ and $H_0 = 72$ km/s/Mpc and a luminosity distance to Coma of 98.4 Mpc. Unless otherwise stated, all uncertainties are given at the 90% confidence level.

2. OBSERVATIONS

The *Suzaku* observation was undertaken as part of AO-1 from 2006 May 31 through June 4, soon after 16 of the 64 PIN diode bias voltages were lowered from 500V to 400V, but before an additional 16 diodes were similarly lowered. We analyze Version 2 of the pre-processed data (PROCV 2.0.6.13), which allows for the diode bias drop, with HEASOFT 6.4.0 and XSPEC 12.4.0w. For the HXD-PIN instrument, the standard data selection criteria are applied to extract the source spectrum, and the same criteria are used to

select times for the modeled non-X-ray background (NXB) spectrum. Specifically, we select observing times when the geomagnetic cut-off rigidity is above a critical value ($COR > 6$ GV), when the satellite is not within the South Atlantic Anomaly ($SAA_HXD = 0$) or has just left it ($T_SAA_HXD > 500$ s), and when *Suzaku* is pointed above and at least 5 degrees away from the Earth's horizon ($ELV > 5^\circ$). The strength of the NXB is known to be roughly inversely proportional to the value of the COR and to be elevated inside the SAA, gradually decaying to typical levels after SAA passage. These criteria ensure that the low NXB of the HXD is minimized and can be well characterized, which is necessary if it is to be accurately modeled. After event selection, the PIN exposure time is reduced from 166.2 ks to 156.1 ks after dead-time correction. The HXD-GSO spectrum is found to be consistent with the background, so we do not consider it further here. We use the *Suzaku* CCD data from the XIS0 chip to check the cross-calibration of *Suzaku* and *XMM-Newton*. Standard event selection was applied to the XIS0 data, leading to an exposure time of 178.7 ks.

The mosaic *XMM-Newton* observations of the Coma cluster, including 14 separate pointings, were done as a part of an instrument performance verification program, a complete log of which is presented in Schuecker et al. (2004). The initial observations were undertaken by and first reported in Briel et al. (2001). Seven new observations, aimed at resolving the temperature structure of the Coma center, have also been performed (PI P. Schuecker). However, high solar activity during the exposures resulted in a high detector background above 2 keV, making these observations less suitable for our purposes, and therefore we use only the observations reported in Section 4 and Table 2 of Schuecker et al. (2004). We choose only to include the EPIC-pn data from *XMM* in our analysis. Because these observations were made early in the mission, they cannot be processed with the standard software, though the EPIC-pn data have undergone in-house processing. Also, its effective area at high energies is higher than for the EPIC-MOS detector, making it the more suitable instrument. The benefit of including the EPIC-MOS data is unclear, due to the addition of cross-calibration errors and given the already high signal-to-noise of the EPIC-pn data.

3. EXTRACTION AND CONSTRUCTION OF SPECTRA

To produce complementary spectra from the *XMM* EPIC-pn and *Suzaku* HXD-PIN data that can be simultaneously fit, the background and responses of both instruments must be carefully considered to minimize systematic uncertainties. The expected non-thermal signal is near the limit of the PIN sensitivity, and a robust characterization of this emission particularly depends on the accuracy of the PIN background and *XMM-Suzaku* cross-normalization.

3.1. HXD-PIN Spectrum and Non-X-ray Background

As the HXD is a non-imaging instrument, we simply extract the PIN spectrum from the selected events and group the spectral bins so that each bin contains at least 30 counts to ensure that Gaussian statistics and χ^2 fitting are valid. The response matrix is provided in the *Suzaku* CALDB⁸ for Version 2 data products, and we use `ae_hxd_pinhnome2_20080129.rsp` for all source components other than the cosmic X-ray background (CXB), for which `ae_hxd_pinflate2_20080129.rsp` is used.

⁸ <http://suzaku.gsfc.nasa.gov/docs/heasarc/caldb/suzaku/>

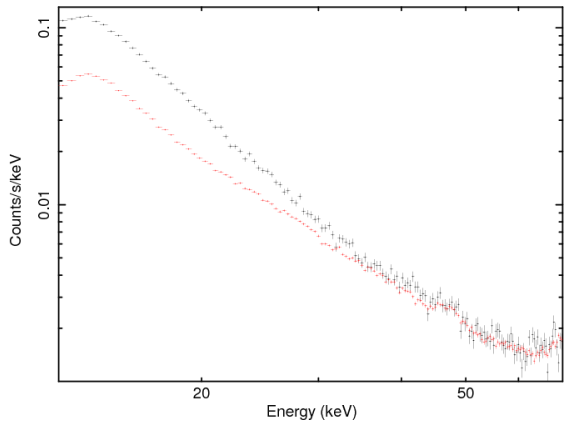


FIG. 1.— *Suzaku* HXD-PIN NXB model spectrum (red data points) compared to the Coma cluster data (uncorrected for background). Note that at energies above 45 keV, the NXB dominates the data and that deviations of the data above the NXB are confined to individual channels that are simply statistical fluctuations or are otherwise imperfectly characterized by the NXB model.

The non-X-ray background for a PIN observation is most accurately obtained from a model, as opposed to a comparable blank field observation. This method is motivated by the strong dependence of the background count rate and spectral shape on the value of the geomagnetic cut-off rigidity (COR) and the time since the passage of the satellite through the South Atlantic Anomaly (SAA), quantities which vary and have a unique distribution for every observation. The model matches the distribution of the COR and other parameters of the observed data. A model is also required because there is no concurrent measurement of the NXB, such as by nodding between Coma and a blank field. We use the so-called “bgd_d” model for Version 2 processed data, which makes use of HXD-GSO information as well as the COR and SAA values. This NXB model is shown with the PIN data spectrum, uncorrected for the background, in Figure 1. While the shape of the NXB is generally well reproduced, the success of the model in determining its overall normalization is $\pm 2.3\%$ from 15–40 keV and $\pm 4\%$ from 40–70 keV (Mizuno et al., *Suzaku* Memo 2008-03⁹). These estimates of the systematic error in the NXB are extrapolated to the 90% confidence interval from the 1σ values derived using Earth-occulted data in *Suzaku* Memo 2008-03. We adopt these values (2.3% from 12–40 keV and 4% from 40–70 keV) as our estimate of the 90% systematic error in the PIN NXB. To confirm the accuracy of the model background, we extracted events for both the data and model for times when the Earth occults the PIN FOV (ELV $< -5^\circ$, all other selection criteria unchanged); the resulting spectra are shown in Figure 2. The fractional difference between the model NXB count rate and the Earth-occulted data is $(0.2 \pm 1.0)\%$ over the energies 12–40 keV and $(-2.0 \pm 2.6)\%$ from 40–70 keV (1σ errors). Over the whole range considered, the fractional difference in count rates is extremely small: $(0.005 \pm 0.9)\%$. Because of the excellent agreement, we do not adjust the level of the background as proposed in Ishida et al., *Suzaku* Memo 2007-10¹⁰.

The estimate of the systematic error adopted here comes from an analysis of Earth-occulted data, which is the same data used to generate models of the NXB. However, it is pos-

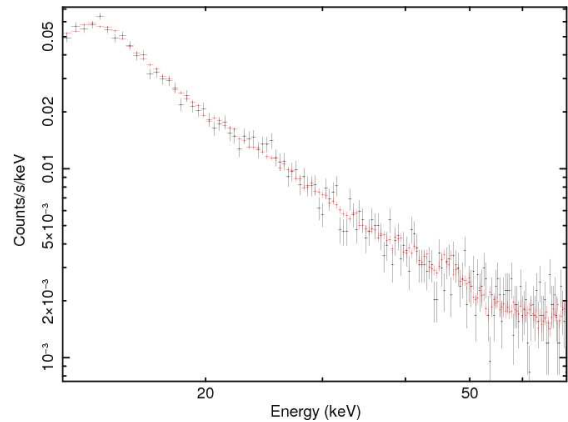


FIG. 2.— *Suzaku* HXD-PIN Earth-occulted data (black data points) compared to the NXB model spectrum for the same time periods of Earth-occultation (red data points). During Earth-occultation, the only events should be due to the NXB. Note that the NXB agrees well with the normalization and shape of the Earth-occulted data at all energies $\gtrsim 12$ keV. (Only this range is used in the spectral fits for Coma.)

sible that a systematic effect could be present during observations of the sky that would not exist during Earth-occulted observations, and so it would not be included in the NXB model or the estimate of the systematic uncertainty. Mizuno et al. (*Suzaku* Memo 2008-03) attempt to test for this possibility with “blank sky” observations and find a larger effective systematic uncertainty. It is clear that some part of this uncertainty is due to the fact that the fields aren’t entirely “blank” and that the source flux will vary field-to-field. Here we refer to relatively bright sources not considered to be part of the more uniform CXB, which has a variance based on the XIS sensitivity to point sources that can be taken into account. When considering many observations of one region on the sky, so that the contamination from sources will vary less, the standard deviation drops from 5.8% derived from many fields to 5.0%, both of which includes a statistical error of about 3.3%. While an additional systematic uncertainty, only in effect when observing the sky, cannot be ruled out, this drop suggests that systematic error estimates derived from sky observations are somewhat conservative. Because the contribution of contaminating sources to systematic error estimates is thus far not well-characterized, we use the value derived from Earth-occulted observations throughout to avoid overestimating this error. We rely on the assumption that a full accounting of contaminating sources would lead to a systematic error estimate similar to our adopted value. However, using the sample of 10 ks exposures of all blank sky observations leads to an estimate of the NXB systematic error of 4%, after subtracting the statistical error and the expected CXB fluctuation (see e.g. Nakazawa et al. 2008). We consider the effect of raising the systematic error to this higher value (for $E < 40$ keV) in § 4.3; our results and conclusions remain qualitatively unchanged.

3.2. XMM EPIC-*pn* Spectrum

To constrain the thermal contribution to the PIN hard X-ray spectrum, it is very helpful to have a spectrum for the same region covered by the HXD-PIN FOV but extending to lower energies where the thermal emission is completely dominant. This low energy spectrum acts as a lever arm on the thermal continuum so that the properties of the thermal gas can be extracted simultaneously with a potential non-thermal component. Because the ICM of Coma is not isothermal and its projected temperature varies across the cluster, a complimen-

⁹ <http://www.astro.isas.ac.jp/suzaku/doc/suzakumemo/suzakumemo-2008-03.pdf>

¹⁰ <http://www.astro.isas.ac.jp/suzaku/doc/suzakumemo/suzakumemo-2007-10.pdf>

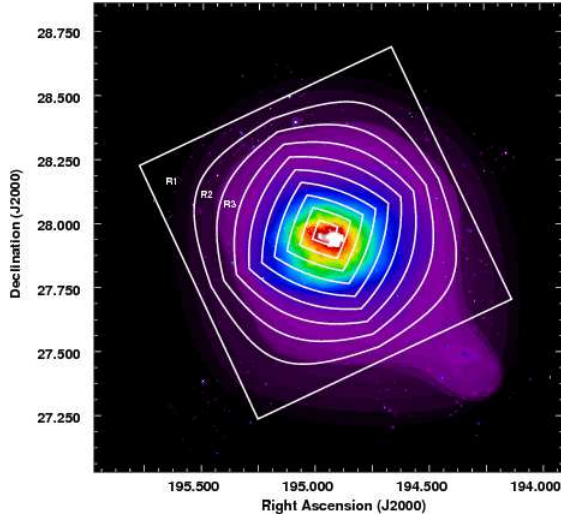


FIG. 3.— *XMM* EPIC-pn 2–7.5 keV wavelet smoothed X-ray surface brightness image (Schuecker et al. 2004) with contours of constant *Suzaku* HXD-PIN effective area overlaid. The contours are spaced at 10% intervals running from 0% to 90% of the effective area for a point source located at the instrument center. In between the contours, the regions labeled R1, R2, etc., correspond to those in Table 1 and in the text.

tary spectrum at softer energies must follow the spatial sensitivity of *Suzaku*'s HXD. Otherwise, localized regions of even slightly hotter gas could mimic the emission of a non-thermal source at hard energies. Since the HXD is made up of 64 individual collimators with optical axes generally aligned to within $4'$ of each other, we approximate the PIN spatial response as a single perfect collimator with a total square FOV of $D = 65'.5$ on a side,

$$R_{\text{coll}} = (D/2 - \theta_x)(D/2 - \theta_y)/(D/2)^2, \quad (3)$$

where R_{coll} is the fraction of the flux detected at angles of (θ_x, θ_y) from the optical axis along the PIN detector axes, relative to a point source located at the center of the HXD FOV ($\theta_x = \theta_y = 0$). We have verified that this model fits the spatial response of the PIN very well. The complimentary *XMM* spectrum is constructed based on this spatial vignetting of the PIN, which is reasonable for our energy range of interest (< 70 keV).

In order to build a spectrum that reflects the PIN vignetting with good statistics, we extract spectra from 10 regions of roughly equal effective area, as shown in Figure 3. The boundaries of the regions are spaced at intervals of 10% of the PIN sensitivity to a central point source. Because the solid angle subtended by a region increases with its distance from the cluster center, it turns out that the count rates of each of these *XMM* spectra are comparable. The same response matrix is used for all spectra, `epn_ef20_sdY7_medium.rsp`, and the auxiliary response files (arfs) for each region are generated in the standard way (Lumb et al. 2003). The background spectrum is derived from the datasets compiled by Read & Ponman (2003), to which we also apply consistent flare cleaning criteria. Before summing these spectra, weighted by the average PIN sensitivity within each region, we scale the arfs so they all agree with the central region (R10) arf at 5 keV, while also scaling the exposure times so the flux remains unchanged. Similarly normalized arfs are required to ensure that the weighted and summed arf will properly represent the response of the final summed spectrum.

We now describe the procedure for creating the summed observed rate spectrum, summed background spectrum, and

corresponding response. Let O_j^i be the observed rate spectrum in spectral channel j for region i , and let B_j^i be the corresponding background spectrum. We constructed the weighted sums

$$\bar{O}_j = \sum_{i=1}^{10} w^i O_j^i, \quad (4)$$

$$\bar{B}_j = \sum_{i=1}^{10} w^i B_j^i, \quad (5)$$

where w^i is the weight of region i in the PIN spectrum, based on the average value of equation (3) inside the region (Table 1), normalized by the PIN nominal central point source sensitivity. Let R_{jk}^i be the response matrix for region i , defined such that given a number flux M_k^i of photons per unit area and time at Earth in spectral channel k , $R_{jk}^i M_k^i$ is the number of events per second observed in spectral channel j . In the nomenclature of X-ray spectral analysis, R_{jk}^i is the ‘‘rsp’’ file for region i . The corresponding average response matrix, \bar{R}_{jk} , must be weighted both by the PIN effective area for the regions (the weights w_i) and by the number of *XMM* photons incident on each area. To include the weighting by the incident flux on each area, we formally assume that to first order the spectra in all 10 regions are described by models M_k^i that have identical spectral shapes given by m_k , but differing normalizations N^i . That is, $M_k^i = N^i m_k$. In our case, we take m_k as an APEC model with $T = 8.2$ keV and abundance relative to solar of 0.24, which is the best fit model to the *XMM-Newton* EPIC-pn spectrum for the entire *Suzaku* PIN FOV. While the temperatures from the outer 5 regions (R5–R1, Table 1) are somewhat inconsistent with our fiducial T , the central regions are weighted more strongly and so it is more important to accurately match their spectral shape than that of the spectra from R5–R1. The average of the temperatures from R10–R1 is in good agreement with previous measurements of Coma’s global temperature (Arnaud et al. 2001; Watanabe et al. 1999). Also, temperatures in R10, R9, and R8 are just consistent at the 90% level with continuum and Fe line ratio fits to the XIS data extracted from those regions, using the method described in Sato et al. (2008). The models M_k^i now differ only in overall flux, given by the APEC normalization N^i , so each observed spectrum can be described as

$$O_j^i - B_j^i = \sum_k R_{jk}^i M_k^i = N^i \sum_k R_{jk}^i m_k. \quad (6)$$

Similarly, we define \bar{R}_{jk} as

$$\bar{O}_j - \bar{B}_j = N \sum_k \bar{R}_{jk} m_k, \quad (7)$$

where N is the APEC normalization of the summed spectrum. Substituting equations (4) and (5) into equation (7) yields, after some algebra,

$$\sum_k \bar{R}_{jk} m_k = \sum_k m_k \sum_i w^i \frac{N^i}{N} R_{jk}^i, \quad (8)$$

so it is clear that

$$\bar{R}_{jk} = \sum_{i=1}^{10} w^i \frac{N^i}{N} R_{jk}^i. \quad (9)$$

TABLE 1
XMM REGIONS AND SPECTRAL FITS

Region	PIN Weight	kT (keV)	Norm. ^a (10^{-2} cm^{-5})
R10	0.933	8.25 ± 0.21	1.67 ± 0.01
R9	0.844	8.33 ± 0.14	4.25 ± 0.02
R8	0.746	8.27 ± 0.15	5.17 ± 0.03
R7	0.647	8.07 ± 0.17	5.09 ± 0.03
R6	0.547	8.07 ± 0.23	4.52 ± 0.04
R5	0.448	7.40 ± 0.34	3.65 ± 0.05
R4	0.348	7.39 ± 0.46	2.93 ± 0.05
R3	0.248	6.99 ± 0.56	2.84 ± 0.06
R2	0.147	7.65 ± 0.44	3.30 ± 0.05
R1	0.0421	7.45 ± 0.68	2.76 ± 0.06

^a Normalization of the APEC thermal spectrum, which is given by $\{10^{-14}/[4\pi(1+z)^2 D_A^2]\} \int n_e n_H dV$, where z is the redshift, D_A is the angular diameter distance, n_e is the electron density, n_H is the ionized hydrogen density, and V is the volume of the cluster.

The value of the weighted normalization N is given by $N = \sum_i w^i N^i$.

For all fits of the *XMM* spectra, the energy range considered differed slightly from the nominal 2-12 keV energy range due to calibration issues. At energies near ~ 2 keV, there exists a sharp edge in the response due to gold in the mirrors, and between 8 and 9 keV there are variable background lines due to copper and zinc. Neither of these features can be sufficiently accounted for given the current calibration, and they tend to become important in regions with very good statistics (all of the Coma *XMM* spectra) and/or regions of low surface brightness particularly near the outer edges of the detector. We avoid these problems by excluding these features and only fitting over the range $2.3 < E < 7.5$ keV and $9.5 < E < 12$ keV. Also, the gain can vary by up to 30 eV, especially during the period when many of these observations took place (Marcus Kirsch, *XMM* Calibration Document¹¹) and the redshift found from fits differs significantly from the nominal value of $z = 0.023$. We fit the gain with a linear function, assuming the redshift to be 0.0232, using the GAIN command in XSPEC for all 10 spectra. We adjusted the gain such that the new response energies E' are related to the original energies by $E' = E/1.00519 + 0.010312$. None of these calibration issues have any important effect on the characterization of the continuum features (IC and hard thermal bremsstrahlung) which are the subject of this paper. However, not including these effects would result in high values of χ^2 for the fits due to the very good statistics in the Coma *XMM* EPIC-pn spectra, and thus make it more difficult to determine the uncertainties in parameters.

Even after these adjustments, fits to the weighted and summed final spectrum with any model produce high chi-squared values ($\chi_{\text{red}}^2 \gtrsim 1.3$). A close inspection of the continuum at various energies reveals that the residuals are slightly larger relative to the errors than would be expected by χ^2 statistics, indicating that we have underestimated the errors. Because of the high signal-to-noise of the Coma observations, the statistical errors no longer completely dominate over channel-to-channel systematic effects, caused by, e.g., differing/variable charge transfer inefficiencies across the detectors and/or between observations, which were obtained over a two year period. We add a 3% systematic error to the

count rate of each channel in the final spectrum to account for these uncertainties, which leads to more reasonable values of $\chi_{\text{red}}^2 \sim 1$.

3.3. XMM EPIC-pn and Suzaku HXD-PIN Cross-Calibration

Joint fits between data from different instruments/missions require a careful consideration of the relative overall calibration if the validity of fits are to be believed. Instead of directly finding the cross-normalization through other observations of a spectrally simple source, such as the Crab, we choose to use the XIS0 chip of the *Suzaku* XRT as an intermediary. An advantage of this method is that it does not require any assumptions about the stability of the absolute calibration of each instrument between calibration observations and our observations. To justify our use of the XIS0 data to calibrate the absolute flux level, we compare the flux observed by XIS0 to the *ROSAT* 0.5-2 keV flux, which was derived using Snowden's ESAS software package (Snowden & Kuntz 1998); these fluxes agree to within 1%.

The overlapping spatial and spectral coverage of the *XMM* EPIC-pn and XIS0 instruments allows a trivial comparison of the flux for a region on the sky. We extract an XIS0 spectrum from the same region as *XMM* spectrum R10, and we generate rmf and arf files for this region using the 2-7.5 keV wavelet-smoothed image created from the *XMM* EPIC-pn data (Schuecker et al. 2004). Though the large XIS PSF ($\sim 2'$) will scatter photons both into and out of this region to a much greater degree than occurs for *XMM*, this effect is accounted for in the arf and tied to the *XMM* data. So while spatial inhomogeneities will not impact the comparison, the shapes of the spectra will not necessarily be identical. The overall flux, however, is not sensitive to small variations in the temperature, and so it provides a good quantity to establish the *XMM*-XIS cross-normalization. For this region, we find that the *XMM* flux is 15% below the XIS0 flux from 2-7.5 keV, and the *XMM* flux, extrapolated to 0.5-2 keV, is similarly 15% below the *ROSAT* flux, and so we scale the summed *XMM* arf by this factor.

The cross-normalization between the XIS chips and the HXD-PIN has been well studied for observations of the Crab nebula (Ishida et al., *Suzaku* Memo 2007-11¹²). We adopt their PIN/XIS0 relative normalization factor of 1.132 ± 0.014 , increasing the PIN arf, and thus lowering the measured flux, by 13.2%.

The associated systematic error for both cross-normalization corrections is estimated to be 1-2%. However, the normalization of the R10 spectrum may differ from that of the other *XMM* region spectra, and also the XIS0-PIN relative normalization may be different due to the fact that Coma is spatially diffuse while the Crab nebula is comparable in size to the XIS resolution. These issues suggest that the true cross-normalization systematic uncertainty is probably larger. We therefore take the combined cross-normalization systematic error to be 5%, which is about as large as can be reasonably allowed by the simple constraint that a model can be continuously fit across the 12 keV boundary between the *XMM* and PIN spectra. Specifically, we vary the cross-normalization until the average of the highest signal-to-noise PIN channels, covering $12 \text{ keV} < E < 16 \text{ keV}$, disagrees with the model by $\sim 2-3\sigma$.

¹¹ <http://xmm2.esac.esa.int/docs/documents/CAL-TN-0018.pdf>

¹² <http://www.astro.isas.ac.jp/suzaku/doc/suzakumemo/suzakumemo-2008-03.pdf>

TABLE 2
FITS TO JOINT *XMM*-PIN SPECTRA

Model	kT (keV)	Norm. ^a (cm ⁻⁵)	Γ or kT (^b)	Norm. ^c	χ^2/dof
Single T	8.45 ± 0.06	0.218 ± 0.001	-	-	1676.05/1689
T+IC ^d	8.42 ± 0.06	0.218 ± 0.001	-1.6	$(4.6 \pm 3.5) \times 10^{-9}$	1671.29/1688
T+IC ^d	8.45 ± 0.07	0.217 ± 0.002	2.0	$(2^{+1.2}_{-2}) \times 10^{-4}$	1676.18/1688
2T ^e	8.0	0.17	10.1	0.05	1672.34/1687
T _{map}	-	-	-	-	1684.35/1690

^a See the note following Table 1.

^b Value is Γ for the T+IC model and kT (in keV) for the 2T model.

^c Value is the normalization of the power-law component for the T+IC model, which is the photon flux at a photon energy of 1 keV in units of photons cm⁻² s⁻¹ keV⁻¹. For the 2T model, the value is the normalization of the second APEC thermal model (see the note following Table 1) in units of cm⁻⁵.

^d Value of Γ is fixed when deriving errors.

^e Parameters unconstrained.

3.4. Cosmic X-ray Background

We modeled the cosmic X-ray background (CXB) spectrum shape following Boldt (1987), specifically using the analytical form proposed by Gruber et al. (1999) based on the *HEAO-1/A2+A4* data. This shape is well-established over the energy range $3 < E < 60$ keV and has been confirmed in subsequent measurements (e.g. Revnivtsev et al. 2003; Churazov et al. 2007; Ajello et al. 2008). We adopt a 10% larger normalization of the spectrum, relative to the original *HEAO-1* determination, to agree with the more recent measurements by *INTEGRAL* (Churazov et al. 2007). This increase is further justified by, and consistent with, the $(8 \pm 3)\%$ higher normalization found with *Swift* (Ajello et al. 2008). Though these most recent measurements lie slightly, but systematically, above the canonical spectrum, as noted by Ajello et al. (2008) they are not inconsistent with other observations at $E > 10$ keV. At the peak of the CXB spectrum, the measurement precision of *HEAO-1* is 10% (Marshall et al. 1980), and the measurement made with the *BeppoSAX* PDS is consistent at the 90% level with a normalization 12% larger (Frontera et al. 2007). In XSPEC, we model the CXB as

$$\text{CXB}(E) = 1.056 \times 10^{-2} \left(\frac{E}{1 \text{ keV}} \right)^{-1.29} e^{-E/(41.13 \text{ keV})}$$

photons cm⁻² s⁻¹ keV⁻¹, (10)

where the normalization is set by a $2^\circ \times 2^\circ$ solid angle of the sky to match the provided response file (see § 3.1).

Cosmic variance due to large scale structure depends on the solid angle of the observation ($\Omega = 0.32 \text{ deg}^2$ for the PIN) and on the cut-off flux of removed point sources (S_{cut}), determined by the *XMM* source completeness (Finoguenov et al. 2004) to be $S_{\text{cut}}(12-70 \text{ keV}) = 2.2 \times 10^{-13} \text{ erg s}^{-1} \text{ cm}^{-2}$. Since the variance $\sigma_{\text{CXB}}/I_{\text{CXB}} \propto \Omega^{-0.5} S_{\text{cut}}^{0.25}$, we can estimate the variance in our observation relative to another measurement assuming a $\log N - \log S$ relation of $N(S) \propto S^{-1.5}$. Using the *HEAO-1 A2* estimate (Shafer 1983; Barcons et al. 2000; Revnivtsev et al. 2003) with $\Omega = 15.8 \text{ deg}^2$, $S_{\text{cut}} = 8 \times 10^{-11} \text{ erg s}^{-1} \text{ cm}^{-2}$, and $\sigma_{\text{CXB}}/I_{\text{CXB}} = 2.8\%$ (1σ), we find a variance of 7.4% (90% confidence), which we take as an additional systematic error in the PIN flux. To account for the 10% discrepancy between the *HEAO-1* and the *INTEGRAL* (Churazov et al. 2007) and *Swift* (Ajello et al. 2008) observations, we also estimate the standard deviation of these measurements to be 7% (90% confi-

dence). Adding these uncertainties in quadrature, we take the total systematic error in the CXB normalization to be 10%. Below 20 keV, the CXB emission is $\lesssim 10\%$ of the total flux, and it just becomes the dominant source of emission at ~ 50 keV.

For the *XMM* data, the background spectra include unresolved point sources that make up the CXB, so they do not need to be modeled.

3.5. Point Sources

Point sources in the *XMM-Newton* Coma mosaic have already been identified by Finoguenov et al. (2004), who also give their count rates in three energy bands (0.5–1 keV, 1–2 keV, and 2–4.5 keV). For each of the 72 sources, we assume the spectrum to be described by an unabsorbed power law and fit this model to each spectrum. We found that the sum of all these models, weighted by w^i according to their positions, could be more concisely described by the sum of two power laws with photon indices 2.1 and 1.6 and normalizations 8.54×10^{-5} and 1.23×10^{-4} photons cm⁻² s⁻¹ keV⁻¹ at 1 keV, respectively. While a simple power law description poorly characterizes some of the sources, care is taken to ensure that individual fits, when extrapolated to high energies, are not unphysical. Their composite spectrum accounts for $\lesssim 1\%$ of the *XMM* flux and is therefore unimportant relative to other systematic effects. For this reason we do not go to the extra effort to exclude the sources from the *XMM* spectra. Assuming the spectral fits are reasonably valid, the point sources account for $\sim 10\%$ of the CXB at PIN energies. During fits of the joint *XMM* and *Suzaku* data, we include this point source composite model for both spectra.

The brightest of these point sources is X Comae, a background AGN with a flux $\sim 10\times$ brighter than any other source in the field. From *XMM* RGS observations, it is known to have a steep spectrum ($\Gamma \sim 2.4$) and to vary in flux by about a factor of 2 over the course of 1 year (Takei et al. 2007). However, due to its position, nearly 90% of the flux from X Comae is not detected by the HXD, so this source does not significantly contribute to the PIN spectrum.

4. SPECTRAL FITS

In our spectral fits, all model components are absorbed by the neutral hydrogen column density toward Coma, $N_H = 9 \times 10^{19} \text{ cm}^2$ [average of values derived from Dickey & Lockman (1990) and Kalberla et al. (2005)], though this absorption is

negligible at energies above 2 keV. In general, we characterize the dominant thermal emission in XSPEC with the APEC model for $E < 40$ keV and with the MeKa model for $E > 40$ keV. In the current version of XSPEC, the APEC and MeKaL models are undefined above 50 keV, though the MeKa and bremsstrahlung models are defined. We tie the parameters of the MeKa model to the APEC parameters, except for the MeKa normalization, which we reduce relative to the APEC normalization by 5.5% to bring the models into agreement at high energies. Also, the abundances relative to solar and the redshift are fixed, to 0.24 and 0.0232 respectively (see § 3.2). This value for the abundance is based on fits to the final weighted and summed *XMM* spectrum alone, and the best-fit abundances of all the individual spectra from the 10 regions is also consistent with this value. Since we are interested in continuum features, the exact choice for the abundance does not strongly affect the results. The spectral fitting results are summarized in Table 2.

4.1. Joint *XMM-Newton* and *Suzaku* Spectral Fits Without Considering Systematic Errors

We simultaneously fit the *Suzaku* HXD-PIN and *XMM-Newton* EPIC-pn spectra for the PIN FOV. First, we consider only a single temperature fit, in order to establish whether the addition of a non-thermal component actually improves the fit (Fig. 4). We find a best fit temperature of 8.45 ± 0.06 keV, which is in general agreement with similar fits to the PIN data (8.3 ± 0.3 keV) and *XMM* data (8.37 ± 0.12 keV) individually. Note that the dip at 15 keV is a known problem with the current NXB model (Mizuno et al., *Suzaku* Memo 2008-03¹³). Since each spectrum is individually described by the same average temperature, the existence of excess emission at hard energies is unlikely. While all of these temperatures are slightly higher than the cluster-wide average temperature of 8.2 keV (Hughes et al. 1993), the energy range in this and similar fits typically extends to energies below 2 keV and thus includes more low temperature gas.

The addition of a power-law non-thermal component produces a formally better description of the spectra, according to the f-test, improving the overall fit (Table 2), but *only* for a photon index $\Gamma < 0$. Allowing the temperature and power law photon index to vary along with each component’s normalization, we find $T = 8.42 \pm 0.06$ keV and $\Gamma = -1.6$, though Γ is poorly constrained. If we fix Γ to this best-fit value, the IC component is significant at the 2.2σ level without considering the effect of systematic uncertainties. However, this photon index is completely inconsistent with the spectral index of the radio halo ($\Gamma \gtrsim 1.8$, Giovannini et al. 1993). While we might expect a flatter spectrum for IC emission, since the hard X-ray photons are emitted by somewhat lower energy electrons than the radio emission, and the radio spectrum flattens at lower frequencies (Thierbach et al. 2003), a rising IC spectrum with energy is completely unexpected and unphysical. The power law fit, in contrast to finding an actual power law signature in the data, is instead compensating for a slight excess at high energies while minimizing its impact on the overall fit at lower energies. Notice that the residuals in Figure 4 above 40 keV lie systematically, if not significantly, above the model. This excess at energies above 40 keV can be explained as a $\sim 2\%$ underestimate of the NXB, as suggested by the Earth-occluded spectrum (see § 3.1). Increasing the background level by 2%

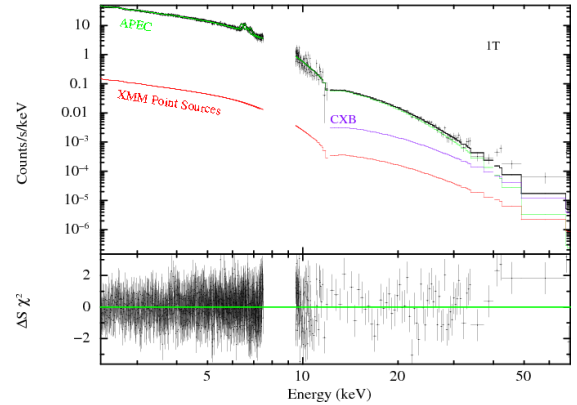


FIG. 4.— *Suzaku* HXD-PIN spectrum ($E > 12$ keV) and the combined *XMM* spectrum ($E < 12$ keV) corresponding to the spatial sensitivity of the PIN. Shown as solid lines are the best fit models for a single temperature thermal component. The thermal model (“APEC”, green) is nearly coincident with the data, though falling below it at higher energies. Also included for all joint fits are the total spectrum for the “*XMM* Point Sources” (red) and the Cosmic X-ray Background (“CXB”, purple), the latter of which only applies to the PIN spectrum since the CXB is subtracted from the *XMM* data along with the NXB.

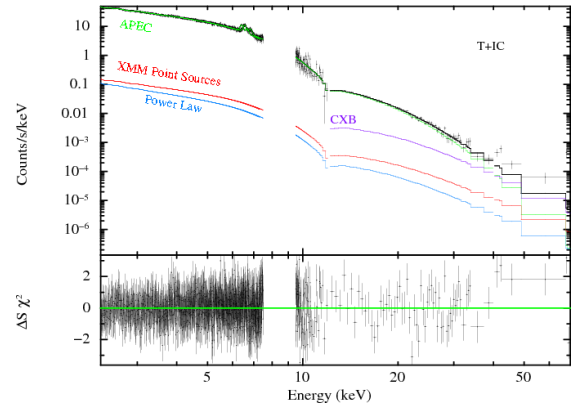


FIG. 5.— *Suzaku* HXD-PIN spectrum ($E > 12$ keV) and the combined *XMM* spectrum ($E < 12$ keV) corresponding to the spatial sensitivity of the PIN. Shown as solid lines are the best fit models for a single temperature thermal component plus a non-thermal component. The thermal model (“APEC”, green) is nearly coincident with the data, though falling below it at higher energies. The non-thermal model (“Power Law”, light blue) is the faintest model component for both spectra, and the photon index is fixed at $\Gamma = 2.0$. The other two components are described in Figure 4.

for $E > 40$ keV results in a best-fit power law component very similar to the model used for the *XMM* point sources, with $\Gamma \sim 1.6$, but it is not significant at even the 1σ level. A similar result is found if the photon index is fixed at $\Gamma = 2$ and the NXB above 40 keV is not increased; this fit is shown in Figure 5. In this case, the fit is not improved by the addition of a power-law component to the model.

Interestingly, a two-temperature model for the ICM yields only a slightly better fit to the data than does the single temperature model (see Fig. 6), though the addition of a second temperature component is probably not formally justified. This result is mainly due to the addition of the 3% systematic error to the *XMM* spectrum. Without including that error, a two-temperature model produces a clearly improved fit over a single temperature model, indicating that the addition of this error is somewhat obscuring evidence for a multi-temperature continuum. In either case, the two temperatures are not strongly constrained, but they are broadly consistent with the spatial variations in Coma’s temperature (see § 4.2

¹³ <http://www.astro.isas.ac.jp/suzaku/doc/suzakumemo/suzakumemo-2008-03.pdf>

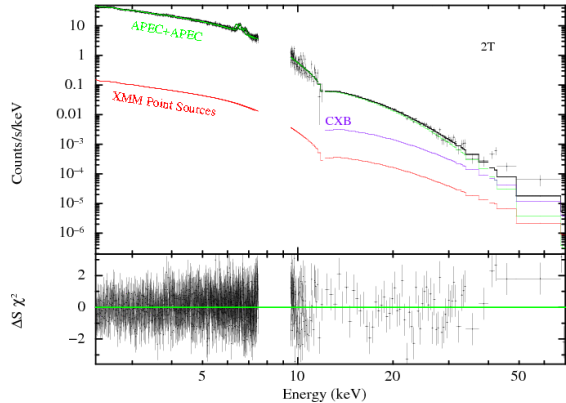


FIG. 6.— *Suzaku* HXD-PIN spectrum ($E > 12$ keV) and the combined *XMM* spectrum ($E < 12$ keV) corresponding to the spatial sensitivity of the PIN. Shown as solid lines are the best fit models for a two-temperature thermal component. The thermal model (“APEC+APEC”, green) is nearly coincident with the data, though falling below it at higher energies. The other two components are described in Figure 4.

and Fig. 7). Therefore, even before systematic errors are considered, the case for the inclusion of a non-thermal component is not strongly motivated.

4.2. Multiple Thermal Components in Coma

In most previous attempts to measure a non-thermal component in the hard spectrum of Coma, the thermal emission was modeled as a single temperature plasma characteristic of the average global state of the ICM. However, Coma is known to host temperature variations (e.g. Honda et al. 1998). Generally, all clusters exhibit a multi-temperature ICM (Cavagnolo et al. 2008), and this is especially true of merging clusters like Coma, which tend to host hot regions due to shocks (Markevitch et al. 1998). At hard energies, where the exponential turnover in the bremsstrahlung continuum is especially well sampled, even weak higher temperature components can significantly contribute to the flux. Also, these components would lead to a higher average temperature for the ICM than if the average cluster temperature were determined from the spectrum at softer energies, such as from 0.5–10 keV.

In the previous section, we found that a two temperature model provided a slightly better description than did a single temperature model of joint fits to the *XMM-Newton* and *Suzaku* data, especially when ignoring the 3% systematic error applied to the *XMM* data. This may indicate that there are multiple temperature components in Coma. The multiple components could occur along the line-of-sight, or in the plane of the sky, or locally (the gas might be multiphase). In fact, previous temperature maps show that Coma certainly has temperature structure which is likely associated with mergers (Watanabe et al. 1999). Here, we test whether this temperature structure alone could reproduce the observed *Suzaku* PIN spectrum of Coma, without any non-thermal emission. From the *XMM-Newton* EPIC-pn mosaic of Coma, we constructed a temperature map on a 16×16 grid with cell size of $4/3$ on a side. Each of the spectra were fit with a single temperature APEC model to produce a temperature map that covers the Coma mosaic, as shown in Figure 7. We weighted these model fits by the PIN spatial sensitivity and combined them. This resulting model was compared to the PIN spectrum (Table 2, row labeled “ T_{map} ”). Note that only the overall normalization of the T_{map} model was allowed to be fit, to compensate for a loss of flux due to incomplete coverage of the map

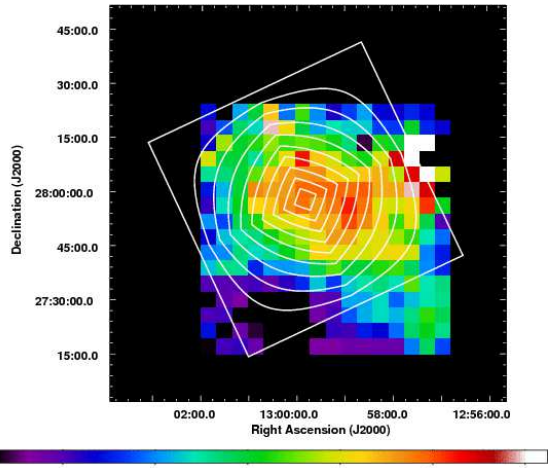


FIG. 7.— *XMM-Newton* temperature map across Coma with HXD-PIN contours of constant PIN effective area overlaid at 10% intervals. The *XMM-Newton* spectra were fit in square spatial regions $4/3$ on a side. The temperatures, given in keV by the color bar, are accurate to either a few tenths of a keV (in the center) or 1–2 keV in lower surface brightness regions. Temperatures shown here were determined from fits to the 0.5–14 keV spectrum in each region.

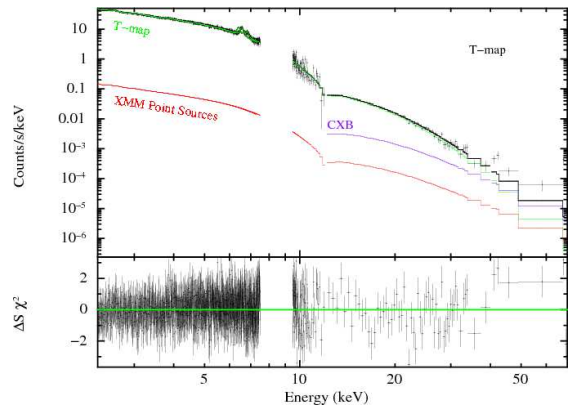


FIG. 8.— *Suzaku* HXD-PIN spectrum ($E > 12$ keV) and the combined *XMM* spectrum ($E < 12$ keV) corresponding to the spatial sensitivity of the PIN. Shown as solid lines are the combined spectra of the best fit models from the temperature map. The thermal model (“ T_{map} ”, green) is nearly coincident with the data, though falling below it at higher energies. The other two components are described in Figure 4.

across the HXD FOV. Also, the spectral shape and normalization of each of the thermal models was the same as given by the *XMM-Newton* temperature, and each model was simply weighted by the average PIN effective area at that position.

This T_{map} model provides a good fit to the PIN spectrum with no adjustable parameters that affect the spectral shape (Fig. 8). While the value of χ^2 is worse than for all previous fits, it is only slightly worse, which is not unexpected since it is not really a fit at all. The fact that *XMM*-derived temperatures extrapolated to PIN energies are sufficient to fully account for the PIN spectrum further suggests that no non-thermal hard X-ray excess has been detected with the PIN, especially below 40 keV and probably below 70 keV. Also, simulating spectra of similar quality to our data, assuming the T_{map} model for the underlying source, yields a joint single temperature fit consistent with that found from the actual data, with $T = 8.51 \pm 0.06$ keV.

4.3. Systematic Errors in the Spectrum

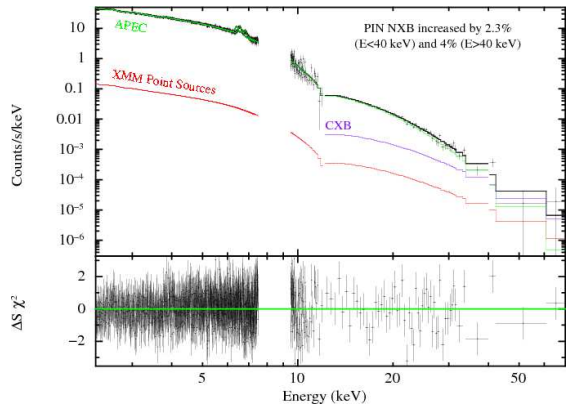


FIG. 9.— *Suzaku* HXD-PIN spectrum ($E > 12$ keV) and the combined *XMM* spectrum ($E < 12$ keV) corresponding to the spatial sensitivity of the PIN. The PIN NXB is increased to its 90% confidence limit, which is 2.3% for $E < 40$ keV and 4% for $E > 40$ keV. The thermal model (“APEC”, green) is nearly coincident with the data, though falling below it at higher energies. The other two components are described in Figure 4. Note that the residuals above the model that exist in the previous fits at $E > 40$ keV have disappeared.

We explicitly consider the systematic error for 3 quantities: the PIN non-X-ray background, the *XMM-Suzaku* cross-normalization factor, and the normalization of the CXB as modeled for the PIN spectrum. To test the effect of these systematic errors, we vary the relevant quantity up and down by our estimate of the 90% systematic error, and evaluate the resulting change in best-fit model parameters. The detection of a non-thermal component cannot be claimed unless it remains robust to variations of these quantities within their systematic errors. Because the largest error is in the normalization of the PIN NXB, we first increase it by 2.3% from 12-40 keV and 4% from 40-70 keV and repeat the single temperature plus non-thermal model fit. The new best-fit IC normalization is pushed to zero. Even before considering the effect of other systematic errors, from this exercise alone it is clear that we *do not detect* non-thermal emission in the HXD-PIN spectrum, given the current uncertainty in the NXB normalization. This fit, with a temperature for the thermal component of 8.33 ± 0.06 keV, is shown in Figure 9. In fact, the value of χ^2 is slightly lower ($\chi^2 = 1672.25$ for 1689 dof) than for the nominal PIN NXB single temperature fit. Notice that the residuals above the model for $E > 40$ keV, seen in all the previous spectral fits, have disappeared.

Though we cannot claim to detect non-thermal emission, we can derive an upper limit to its flux based on joint fits to the spectra, including systematic errors in the following way. First, for an assumed photon index which we fix, we find the nominal normalization N_{nom} and corresponding 90% upper bound $N_{\text{nom}}^{\text{ul}}$ of the non-thermal component for a single temperature plus power law model, allowing the temperature and normalization of the thermal component to vary. Then, for each systematically uncertain quantity, we set that quantity to the limit bounded by the systematic error in the sense that increases the value of the non-thermal normalization $N_{\text{sys},i}$, and we fit for it and its 90% upper bound $N_{\text{sys},i}^{\text{ul}}$. The statistical and systematic errors of the power law normalization are then given by

$$\delta_{\text{stat}} = N_{\text{nom}}^{\text{ul}} - N_{\text{nom}}, \quad (11)$$

and

$$\delta_{\text{sys},i} = N_{\text{sys},i}^{\text{ul}} - N_{\text{nom}}^{\text{ul}} = N_{\text{sys},i} - N_{\text{nom}}, \quad (12)$$

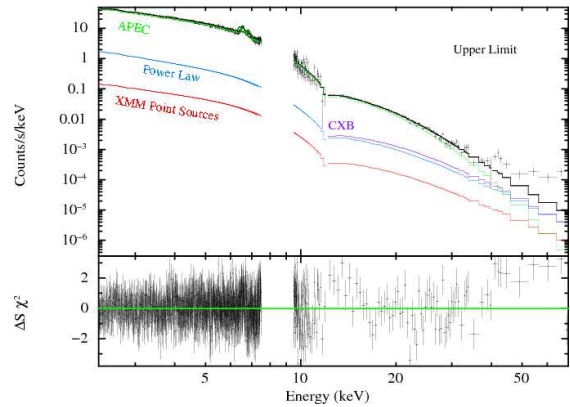


FIG. 10.— *Suzaku* HXD-PIN spectrum ($E > 12$ keV) and the combined *XMM* spectrum ($E < 12$ keV) corresponding to the spatial sensitivity of the PIN. All quantities with systematic uncertainties (PIN CXB and NXB, the *XMM-Suzaku* cross calibration) are set to their 90% confidence limit in the direction that favors the addition of a power law model component to describe the data. The thermal model (“APEC”, green) is nearly coincident with the data, though falling below it at higher energies. The non-thermal model (“Power Law”, light blue) is shown for $\Gamma = 2$ at its 90% confidence upper limit value. The other two components are described in Figure 4. respectively. The final 90% upper limit is then given by

$$N_{\text{tot}}^{\text{ul}} = N_{\text{nom}} + \sqrt{\sum_i \delta_{\text{sys},i}^2 + \delta_{\text{stat}}^2}. \quad (13)$$

We add each systematic error contribution in quadrature because it is unlikely that we chose normalizations for these 3 quantities such that each one disfavors the detection of non-thermal emission in the most severely possible way.

The upper limits for a range of assumed photon indices is provided in Table 3, and in Figure 10 we show, for $\Gamma = 2$, the resulting best fit with all 3 systematic quantities set at the limit of their 90% confidence range. Over the PIN energy band (12-70 keV), the flux is relatively independent of photon index. To compare our results to the most recent previous detections of non-thermal emission in Coma, we also give the upper limit on the non-thermal flux in the 20-80 keV band, which is 6.0×10^{-12} erg $\text{s}^{-1} \text{cm}^{-2}$ for $\Gamma = 2$. This limit is inconsistent with the *RXTE* (Rephaeli & Gruber 2002) and *BeppoSAX* (Fusco-Femiano et al. 2004) detections by about a factor of 2.5, but at the same level as the upper limit derived by Rossetti & Molendi (2004) from the *BeppoSAX* data. If we adopt a 4% systematic error for the PIN NXB instead of 2.3% for $E < 40$ keV, which would better agree with that derived from “blank sky” observations, then our upper limit increases by 35%. Similarly, if we also increase the CXB and *XMM-Suzaku* cross-normalization to 18% and 10%, respectively, our upper limit for $\Gamma = 2$ would increase by 50%. In either case, our upper limit still excludes the *RXTE* and *BeppoSAX* detections, if FOV differences are ignored (see § 5 for a more meaningful comparison).

5. IMPLICATIONS AND DISCUSSION

After modeling all the known possible contributions to the 2–70 keV spectrum, simultaneously fitting for the parameters of thermal and non-thermal spectral components, and taking into account the systematic uncertainty of the PIN NXB, we do not see evidence for IC emission in Coma at our level of sensitivity. We therefore derive an upper limit to non-thermal, hard X-ray emission through a careful consideration of the maximum effect of systematic uncertainties on our ability to detect a non-thermal signal.

TABLE 3
90% UPPER LIMITS ON IC FLUX

Γ	Norm. ^a (10^{-3} photons keV ⁻¹ cm ⁻² s ⁻¹)	Flux (12-70 keV) (10^{-12} erg s ⁻¹ cm ⁻²)	Flux (20-80 keV) (10^{-12} erg s ⁻¹ cm ⁻²)	<i>BeppoSAX</i> Detection ^b (10^{-12} erg s ⁻¹ cm ⁻²)
1.0	0.155	14.4	14.9	
1.1	0.220	14.2	14.4	
1.2	0.311	14.1	13.9	
1.3	0.439	13.9	13.4	
1.4	0.617	13.8	12.9	
1.5	0.860	13.5	12.3	
1.6	1.18	13.1	11.6	
1.7	1.58	12.4	10.7	
1.8	2.04	11.4	9.51	
1.9	2.48	9.83	7.98	
2.0	2.70	7.64	6.01	15 ± 5
2.1	2.70	5.46	4.15	
2.2	2.56	3.71	2.73	
2.3	2.36	2.46	1.74	
2.4	2.15	1.62	1.11	

^a Normalization of the power-law component for the T+IC model, which is the photon flux at a photon energy of 1 keV.

^b Flux (20-80 keV), as reported in Fusco-Femiano et al. (2004).

This conservative upper limit is similar to that derived by Rossetti & Molendi (2004) and is inconsistent with claimed detections using *RXTE* (Rephaeli & Gruber 2002) and *BeppoSAX* (Fusco-Femiano et al. 2004) by approximately a factor of 2.5. However, it should be noted that we do not include potentially lost emission due to PIN vignetting from any of our flux upper limits relative to the larger FOVs of *RXTE* and *BeppoSAX*, which have collimator FWHM of 1° and 1.3°, respectively.

If IC emission follows the radio synchrotron emission [as derived from the point source-subtracted radio image from Deiss et al. (1997)], as it would for a uniform B field throughout the cluster, our upper limits imply a total IC flux 1.7–2× larger would be found inside an *RXTE/BeppoSAX*-like FOV. We also consider a more detailed spatial distribution for the underlying IC emission, derived from the re-acceleration model of Brunetti & Blasi (2005), in which relativistic protons collide with electrons in the ICM that are then re-accelerated by Alfvén waves due to cluster mergers. Given the radio spectrum of Coma, this model predicts that the smaller FOV of the *Suzaku* HXD-PIN would lead to an underestimate of the non-thermal flux by a factor of 2–2.5 (possibly 3 under extreme circumstances). If this model for the spatial distribution of the non-thermal emission is correct, then our upper limit is just consistent with the measurements of Rephaeli & Gruber (2002) and Fusco-Femiano et al. (2004). (However, the Brunetti & Blasi (2005) model actually predicts a non-thermal flux considerably below the *BeppoSAX* and *RXTE* detections.) Because any spatial variation of the magnetic field strength is unknown, a direct comparison between these missions is not possible with any precision. Under the reasonable assumption that B decreases with radius, our upper limit will be $\gtrsim 2\times$ larger, so our result cannot definitively rule out the detections discussed above. Regardless of this issue, the upper limit is approximately the same as or slightly higher than the upper limit range found by Rossetti & Molendi (2004).

However, the *BeppoSAX* PDS measures a 20-80 keV flux for the Crab of 1.23×10^{-8} erg s⁻¹ cm⁻² (Kirsch et al. 2005), while the *Suzaku* PIN flux over this energy range is 1.56×10^{-8} erg s⁻¹ cm⁻², after applying the 13.2% correction to bring

the PIN spectrum into agreement with the XIS fluxes (Ishida et al., *Suzaku* Memo 2007-11¹⁴). This 21% flux difference implies our upper limit would be 4.7×10^{-12} erg s⁻¹ cm⁻² on the *BeppoSAX* scale, which is on the lower end of the range estimated by Rossetti & Molendi (2004). Also, even if we only detect one-third of the total emission observed by the *BeppoSAX* PDS, we would just barely exclude the nominal value of the Fusco-Femiano et al. (2004) measurement.

Assuming the differing measurements of non-thermal emission are not due to the IC radiation having a larger extent, what might be the cause of this discrepancy? While it could be explained by a greater point source contamination at hard energies for the *RXTE* and *BeppoSAX* missions due to their larger FOVs, most likely we differ in our results because of different considerations of the thermal gas. For both detections, the gas temperature was found to be lower than our nominal value of 8.45 keV. Fixing the gas temperature to their assumed values in our fits yields a $\Gamma = 2.0$ non-thermal component significance $> 4\sigma$, without including systematic effects, for $T = 7.67$ keV (*RXTE*) and $T = 8.2$ keV (*BeppoSAX*); however, these fits are poor relative to fits in which the temperature is a free parameter. Though these temperatures differ from our best-fit value by only a few percent, the exponential decline of bremsstrahlung continuum at high energies amplifies even small differences. The lower measurements of the ICM temperature appear not to be due to the inclusion of data at low energies ($E < 1$ keV), which can bias average temperature estimates low. Most likely, the larger FOVs of *RXTE* and *BeppoSAX* allowed the inclusion of emission from more cool gas in the cluster outskirts than was observed by *Suzaku*. This emission would serve to lower the average observed temperature, which is primarily determined from emission at lower energies ($E < 10$ keV). But, as evidenced by the temperature map in Figure 7, a distribution of higher-than-average temperature regions can effectively increase the average gas temperature observed at high energies, as first seen by Neumann et al. (2003).

We take the reasonably good agreement between the thermal models derived from the *XMM* temperature map and the

¹⁴ <http://www.astro.isas.ac.jp/suzaku/doc/suzakumemo/suzakumemo-2007-11.pdf>

PIN spectrum to mean that we essentially only detect thermal emission from Coma out to 70 keV. This result is fully consistent with recent *INTEGRAL* detections of extended hard X-ray emission. Renaud et al. (2006) performed a point-by-point spectral comparison between *XMM*-derived and *INTEGRAL*-derived temperatures and found that they followed a strict one-to-one correlation. Similarly, Eckert et al. (2007a) characterized a surface brightness excess relative to the *XMM* data, which they found to be best described by extended hot, thermal emission at a $T \sim 12 \pm 2$ keV. This excess coincides with the hotter temperatures ($T \sim 10$ – 11 keV) to the west of the PIN pointing center in Figure 7.

From our upper limit on the flux of IC emission, we can derive a lower limit on the average magnetic field strength B as shown by Harris & Romanishin (1974). Equation (2) refers to the total energy emitted for one electron; it is more useful to consider the ratio of monochromatic fluxes $F_R(\nu_R)$, $F_X(\nu_X)$ at frequencies ν_R , ν_X , for a power law distribution of electrons, from which we can derive an expression for the magnetic field as

$$B = C(p)(1+z)^{(p+5)/(p+1)} \left(\frac{F_R}{F_X}\right)^{2/(p+1)} \left(\frac{\nu_R}{\nu_X}\right)^{(p-1)/(p+1)}, \quad (14)$$

where p is the index of the electron distribution $N(E) \propto E^{-p}$ and is related to the spectral index α ($F_\nu \propto \nu^{-\alpha}$) by $p = 2\alpha + 1$. The value of the proportionality constant $C(p)$ can be found from the ratio of the synchrotron flux (Longair 1994, eqn. 18.49) to the IC flux (Rybicki & Lightman 1979, eqn. 7.31). Assuming that the electron energy distribution does not turn over significantly at low energies and that $\alpha = 1$, we find $B > 0.15 \mu\text{G}$. This limit is still below the equipartition value of $0.5 \mu\text{G}$ (Giovannini et al. 1993), and it is well below the line-of-sight estimates of a few μG derived from Faraday rotation measure (RM) studies (Feretti et al. 1995). Note that the Faraday RM magnetic field estimates are sensitive to the B field geometry and may imply a field strength larger than the volume-averaged value if B is preferentially aligned along filamentary structures on small scales (Petrosian 2001). Also, we are unable to put interesting constraints on the relativistic energy budget of Coma, since our lower limit includes the equipartition estimate of B , which defines the minimum energy in relativistic components and would not imply a significant contribution to the energy budget of Coma.

It has been noted that the hard excess detected by Eckert et al. (2007a) also corresponds to the peak in the point source-subtracted image from Deiss et al. (1997), potentially indicating that the hard emission could in fact be non-thermal

in origin (Eckert et al. 2007b). In fact, we suspect that this peak, which appears tantalizingly like a small radio relic, is not a true feature of the halo, but instead is the result of imperfect source subtraction. Due to the large beam size used to create the diffuse radio image, extended emission from radio galaxies might not have been properly subtracted using a point source list. We point out that the strongest radio source (1256+282 or 5C 4.81, centered on NGC 4869) in Coma is near this position, is a head-tail radio galaxy with a steeper spectral index than rest of the halo (Giovannini et al. 1993), and that its tail extends to the west (O’Dea & Owen 1985, see Fig. 1(j)) and turns north (Venturi et al. 1990, see Fig. 2). Subtracting a point source from this morphology would leave a residual very similar to that in the Deiss image. Therefore, any relation between the location of hard emission and this radio feature probably should be regarded as coincidence.

As the calibration of the NXB model improves, constraints on IC emission in Coma will tighten, possibly leading to a detection. The uncertainty in the current background model, “bgd_d,” is more than a factor of 2 lower than the original model. However, the existence of non-thermal emission in the Coma cluster may have to be determined by future missions — particularly, those missions with hard X-ray imaging capabilities like NuStar¹⁵, Astro-H (previously NeXT)¹⁶, and Simbol-X¹⁷. If the IC emission is localized, then our joint fitting-technique can be used for many much smaller regions where temperature-mixing will be less significant and the IC component will be relatively stronger. Also, the B field strength can be derived spatially across a cluster, yielding a better estimate of the possible pressure support provided by relativistic components in the ICM, which could modify mass estimates that depend on the hydrostatic equilibrium state of the cluster gas.

We thank W. Reich who kindly provided us with the Deiss et al. (1997) radio image. We thank M. Ajello, G. Brunetti, F. Fusco-Femiano, S. Molendi, and P. Rebusco for useful discussions. Also, we are grateful to the referee for helpful comments that improved the paper. Support for this work was provided by NASA *Suzaku* grants NNX06AI44G and NNX06AI37G and *XMM-Newton* grant NNX06AE76G. DRW was supported by a Dupont Fellowship and a Virginia Space Grant Consortium Fellowship. AF was partially supported by NASA NNG05GM5OG grant to UMBC. Basic research in radio astronomy at the NRL is supported by 6.1 Base funding.

¹⁵ <http://www.nustar.caltech.edu/>

¹⁶ <http://www.astro.isas.ac.jp/future/NeXT/>

¹⁷ <http://www.asdc.asi.it/simbol-x/>

REFERENCES

- Ajello, M., et al. 2008, *ApJ*, 689, 666
 Ajello, M., et al. 2009, *ApJ*, 690, 367
 Arnaud, M., et al. 2001, *A&A*, 365, L67
 Barcons, X., Mateos, S., & Ceballos, M. T. 2000, *MNRAS*, 316, L13
 Bazzano, A., et al. 1990, *ApJ*, 362, L51
 Boldt, E. 1987, *Observational Cosmology*, 124, 611
 Briel, U. G., et al. 2001, *A&A*, 365, L60
 Brunetti, G., & Blasi, P. 2005, *MNRAS*, 363, 1173
 Buote, D. A. 2001, *ApJ*, 553, L15
 Cavagnolo, K. W., Donahue, M., Voit, G. M., & Sun, M. 2008, *ApJ*, 682, 821
 Churazov, E., et al. 2007, *A&A*, 467, 529
 Deiss, B. M., Reich, W., Lesch, H., & Wielebinski, R. 1997, *A&A*, 321, 55
 Dickey, J. M., & Lockman, F. J. 1990, *ARA&A*, 28, 215
 Eckert, D., Neronov, A., Courvoisier, T. J.-L., & Produit, N. 2007a, *A&A*, 470, 835
 Eckert, D., Produit, N., Neronov, A., & Courvoisier, T. J.-L. 2007b, *ArXiv e-prints*, 710, arXiv:0710.4417
 Eckert, D., Produit, N., Paltani, S., Neronov, A., & Courvoisier, T. J.-L. 2008, *A&A*, 479, 27
 Feretti, L., Dallacasa, D., Giovannini, G., & Tagliani, A. 1995, *A&A*, 302, 680
 Finoguenov, A., Briel, U. G., Henry, J. P., Gavazzi, G., Iglesias-Paramo, J., & Boselli, A. 2004, *A&A*, 419, 47
 Frontera, F., et al. 2007, *ApJ*, 666, 86

- Fujita, Y., et al. 2008, *PASJ*, 60, 1133
- Fusco-Femiano, R., dal Fiume, D., Feretti, L., Giovannini, G., Grandi, P., Matt, G., Molendi, S., & Santangelo, A. 1999, *ApJ*, 513, L21
- Fusco-Femiano, R., Orlandini, M., Brunetti, G., Feretti, L., Giovannini, G., Grandi, P., & Setti, G. 2004, *ApJ*, 602, L73
- Fusco-Femiano, R., Landi, R., & Orlandini, M. 2007, *ApJ*, 654, L9
- Giovannini, G., Feretti, L., Venturi, T., Kim, K.-T., & Kronberg, P. P. 1993, *ApJ*, 406, 399
- Gruber, D. E., Matteson, J. L., Peterson, L. E., & Jung, G. V. 1999, *ApJ*, 520, 124
- Harris, D. E., & Romanishin, W. 1974, *ApJ*, 188, 209
- Henriksen, M. J., & Mushotzky, R. F. 1986, *ApJ*, 302, 287
- Honda, H., Hirayama, M., Ezawa, H., Kikuchi, K., Ohashi, T., Watanabe, M., Kunieda, H., & Yamashita, K. 1998, *The Hot Universe*, 188, 308
- Hughes, J. P., Butcher, J. A., Stewart, G. C., & Tanaka, Y. 1993, *ApJ*, 404, 611
- Kalberla, P. M. W., Burton, W. B., Hartmann, D., Arnal, E. M., Bajaja, E., Morras, R., Pöppel, W. G. L. 2005, *A&A*, 440, 775
- Kirsch, M. G., et al. 2005, *Proc. SPIE*, 5898, 22
- Longair, M. S. 1994, Cambridge: Cambridge University Press, 1994, 2nd ed.
- Lumb, D. H., Finoguenov, A., Saxton, R., Aschenbach, B., Gondoin, P., Kirsch, M., & Stewart, I. M. 2003, *Proc. SPIE*, 4851, 255
- Lutovinov, A. A., Vikhlinin, A., Churazov, E. M., Revnivtsev, M. G., & Sunyaev, R. A. 2008, *ArXiv e-prints*, 802, arXiv:0802.3742
- Mantz, A., Allen, S. W., Ebeling, H., & Rapetti, D. 2008, *MNRAS*, 387, 1179
- Markevitch, M., Forman, W. R., Sarazin, C. L., & Vikhlinin, A. 1998, *ApJ*, 503, 77
- Marshall, F. E., Boldt, E. A., Holt, S. S., Miller, R. B., Mushotzky, R. F., Rose, L. A., Rothschild, R. E., & Serlemitsos, P. J. 1980, *ApJ*, 235, 4
- Mitsuda, K., et al. 2007, *PASJ*, 59, 1
- Nakazawa, K., et al. 2008, arXiv:0812.1438
- Neumann, D. M., Lumb, D. H., Pratt, G. W., & Briel, U. G. 2003, *A&A*, 400, 811
- Nevalainen, J., Oosterbroek, T., Bonamente, M., & Colafrancesco, S. 2004, *ApJ*, 608, 166
- O'Dea, C. P., & Owen, F. N. 1985, *AJ*, 90, 927
- Okajima, T., et al. 2008, *ApJ*, submitted
- Petrosian, V. 2001, *ApJ*, 557, 560
- Randall, S. W., Sarazin, C. L., & Ricker, P. M. 2002, *ApJ*, 577, 579
- Read, A. M., & Ponman, T. J. 2003, *A&A*, 409, 395
- Renaud, M., Bélanger, G., Paul, J., Lebrun, F., & Terrier, R. 2006, *A&A*, 453, L5
- Rephaeli, Y. 1977, *ApJ*, 212, 608
- Rephaeli, Y., Ulmer, M., & Gruber, D. 1994, *ApJ*, 429, 554
- Rephaeli, Y., & Gruber, D. 2002, *ApJ*, 579, 587
- Revnivtsev, M., Gilfanov, M., Sunyaev, R., Jahoda, K., & Markwardt, C. 2003, *A&A*, 411, 329
- Ricker, P. M., & Sarazin, C. L. 2001, *ApJ*, 561, 621
- Ritchie, B. W., & Thomas, P. A. 2002, *MNRAS*, 329, 675
- Rossetti, M., & Molendi, S. 2004, *A&A*, 414, L41
- Rybicki, G. B., & Lightman, A. P. 1979, New York: Wiley-Interscience, 1979
- Sarazin, C. L. 1988, Cambridge Astrophysics Series, Cambridge: Cambridge University Press, 1988
- Sarazin, C. L. 1999, *ApJ*, 520, 529
- Sato, T., et al. 2008, in preparation
- Schuecker, P., Böhringer, H., Reiprich, T. H., & Feretti, L. 2001, *A&A*, 378, 408
- Schuecker, P., Finoguenov, A., Miniati, F., Böhringer, H., & Briel, U. G. 2004, *A&A*, 426, 387
- Shafer, R. A. 1983, PhD. Thesis, University of Maryland
- Skillman, S. W., O'Shea, B. W., Hallman, E. J., Burns, J. O., & Norman, M. L. 2008, *ApJ*, 689, 1063
- Snowden, S. L., & Kuntz, K. D. 1998, "Cookbook for analysis procedures for ROSAT XRT/PSPC observations of extended objects and diffuse background"
- Takahashi, T., et al. 2007, *PASJ*, 59, 35
- Takei, Y., Henry, J. P., Finoguenov, A., Mitsuda, K., Tamura, T., Fujimoto, R., & Briel, U. G. 2007, *ApJ*, 655, 831
- Thierbach, M., Klein, U., & Wielebinski, R. 2003, *A&A*, 397, 53
- Venturi, T., Giovannini, G., & Feretti, L. 1990, *AJ*, 99, 1381
- Watanabe, M., Yamashita, K., Furuzawa, A., Kunieda, H., Tawara, Y., & Honda, H. 1999, *ApJ*, 527, 80
- Wik, D. R., Sarazin, C. L., Ricker, P. M., & Randall, S. W. 2008, *ApJ*, 680, 17
- Willson, M. A. G. 1970, *MNRAS*, 151, 1